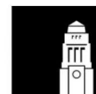

UNIVERSITY OF LEEDS

This is a repository copy of *Design and simulation of InGaAs/AlAsSb quantum-cascade lasers for short wavelength emission*.

White Rose Research Online URL for this paper:
http://eprints.whiterose.ac.uk/1109/

Article:

Evans, C.A., Jovanovic, V.D., Indjin, D. et al. (2 more authors) (2005) Design and simulation of InGaAs/AlAsSb quantum-cascade lasers for short wavelength emission. Applied Physics Letters, 87 (141109). ISSN 0003-6951

https://doi.org/10.1063/1.2067701

Reuse
See Attached

Takedown
If you consider content in White Rose Research Online to be in breach of UK law, please notify us by emailing eprints@whiterose.ac.uk including the URL of the record and the reason for the withdrawal request.

eprints@whiterose.ac.uk
https://eprints.whiterose.ac.uk/

White Rose Consortium ePrints Repository
http://eprints.whiterose.ac.uk/

This is an author produced version of a paper published in **Applied Physics Letters**.

White Rose Repository URL for this paper:
http://eprints.whiterose.ac.uk/archive/00001109/

Citation for the published paper
Evans, C.A. and Jovanovic, V.D. and Indjin, D. and Ikonic, Z. and Harrison, P. (2005) *Design and simulation of InGaAs/AlAsSb quantum-cascade lasers for short wavelength emission.* Applied Physics Letters, 87 (141109).

Repository paper
Evans, C.A. and Jovanovic, V.D. and Indjin, D. and Ikonic, Z. and Harrison, P. (2005) *Design and simulation of InGaAs/AlAsSb quantum-cascade lasers for short wavelength emission.*
Author manuscript available at: http://eprints.whiterose.ac.uk/archive/00001109/

White Rose Consortium ePrints Repository
eprints@whiterose.ac.uk

Design and simulation of InGaAs/AlAsSb quantum cascade lasers for short wavelength emission

C. A. Evans, V. D. Jovanović, D. Indjin, Z. Ikonić, and P. Harrison
School of Electronic and Electrical Engineering, University of Leeds, Leeds LS2 9JT, United Kingdom

The design and simulation of an $In_{0.53}Ga_{0.47}As/Al_{0.56}As_{0.44}Sb$ quantum cascade laser emitting in the near-infrared is presented. Designed using a self-consistent rate equation solver coupled with an energy balance rate equation, the proposed laser has a calculated population inversion of ∼20 % at 77 K and sufficient gain to achieve room-temperature laser emission at $\lambda \sim 2.8$ μm. Threshold currents in the range 4–8 kA/cm^2 are estimated as the temperature increases from 77 K to 300 K. The output characteristics of the proposed laser are compared to an existing $\lambda \sim 3.1$ μm $In_{0.53}Ga_{0.47}As/Al_{0.56}As_{0.44}Sb$ quantum cascade structure presented in the literature.

The $In_{0.53}Ga_{0.47}As/Al_{0.56}As_{0.44}Sb$ material system appears to be the prime candidate for realising high-performance quantum cascade lasers (QCLs) with short emission wavelengths [1–3]. The wavelength limit of a QCL is ultimately set by the conduction band offset of the material system, and in $In_{0.53}Ga_{0.47}As/Al_{0.56}As_{0.44}Sb$ heterostructures has a value of ∼1.6 eV. This value of the band offset should provide enough quantum confinement to achieve laser emission in the 3–5 μm atmospheric transmission window, which is of interest due to the potential applications in freespace optical communication links. $In_{0.53}Ga_{0.47}As/Al_{0.56}As_{0.44}Sb$ is lattice matched to InP which is a favourable property since optical confinement can be provided using well-understood InP-based waveguides. Revin *et al.* have reported intersubband electroluminescence in the range $\lambda \sim 3.1$–5.3 μm from InGaAs/AlAsSb QC structures [1, 2] and have observed pulsed mode laser emission at $\lambda \sim 4.3$ μm up to a maximum temperature of 240 K [3]. 3.1 μm is currently the shortest spontaneous emission wavelength observed from an intersubband device [1]. Room-temperature electroluminescence at ∼ 4.5 μm from InGaAs/AlAsSb QC structures [4] has recently been reported by Yang *et al.*, who have also demonstrated InGaAs/AlAsSb QCLs emitting at the same wavelength with maximum operating temperatures of up to 400 K in pulsed mode [5]. Thorough investigation of the carrier dynamics in Sb-based quantum cascade structures as well as further improvements in the QCL design are required to approach the goal of achieving above-room temperature near-infrared ($\lambda \sim 3\mu$m) laser emission.

In this letter, two main topics are addressed: (i) simulation of electronic transport and electron heating in Sb-based QC structures using a fully self-consistent scattering rate model and (ii) the development of a short wavelength (∼3 μm) InGaAs/AlAsSb QCL using conclusions drawn from the simulation of the 3.1 μm electroluminescence InGaAs/AlAsSb structure presented in the literature (from this point on referred to as structure A) as a frame of reference [1].

To simulate the QC structures using the self-consistent rate equation model [6], the electron energies and wavefunctions were obtained by solving the Schrödinger equation within the envelope function and effective mass approximations with the energy dependent effective mass taken into account via Kane's two-band model. The wavefunctions were then used to evaluate all the principal electron-electron and electron-LO phonon intra- and inter-period scattering rates [7]. An energy balance equation was also included in the self-consistent procedure [8] from which the electron temperature (T_e) can be evaluated. The self-consistent solution yields the nonequilibrium

TABLE I: Calculated subband populations in the structures. ULL: upper laser level, LLL: lower laser level, GL: ground level, LIL: lowest injector level.

Structure	**A**	**B**	**B**	**B**	**B**
F [kV/cm]	128	130	130	130	130
T [K]	77	77	77	300	300
N_s [cm^{-2}]	2.4×10^{11}	2.4×10^{11}	3.8×10^{11}	2.4×10^{11}	3.8×10^{11}
State	**Populations [%]**				
ULL	4.3	23.8	22.1	12.2	12.4
LLL	1.7	3.8	4.1	3.8	4.2
GL	53.3	5.8	5.9	5.2	5.2
LIL	21.2	18.1	17.2	12.5	12.4

electron density in each of the subbands, from which the total current density J, the local gain g and the modal gain G_M can be calculated. Based on the estimation of waveguide parameters i.e. the confinement factor Γ, wavegude losses α_W and mirror losses α_M, the threshold current can be determined.

Structure A was analysed using the material parameters given in Refs. 9 and 10. Table I lists the calculated electron densities in the active region levels and the lowest injector state as a percentage of the total number of electrons in one period. At the design field of 128 kV/cm at a lattice temperature of 77 K, over 50% of the carriers in structure A are trapped in the active region ground level due to the minimal overlap with the uppermost injector state wavefunctions. This 'bottleneck' effect prevents efficient injection into the injector miniband, significantly reducing the population inversion (∼ 2.6%). The calculated F–J curve at 77 K is shown as the dashed line in Fig. 1. The device saturates at a current density of ∼2 kA/cm^2, in agreement with the experimentally measured I–V characteristics which become unstable above this value [1]. The waveguide described in Ref. 1 was analysed using a transfer-matrix technique [11] and the modal gain calculated using the mode confinement factor ($\Gamma = 41\%$) (inset Fig. 1). The mirror losses of ∼7 cm^{-1} were estimated using $\alpha_M = -1/L \ln R_1 R_2$ (where L is the length of the laser structure and R_1 and R_2 are the reflectivities at ends of the structure) and added to the calculated α_W (∼3 cm^{-1}) to give total losses of ≈10 cm^{-1}, as denoted by the horizontal dotted line in the inset of Fig. 1. As shown in the inset of Fig. 1, there is insufficient gain in structure A to overcome the total losses and achieve laser emission, which in is agreement with experimental findings [1].

A new structure (denoted as structure B; see Fig. 2) was designed with the aim of improving electron transport

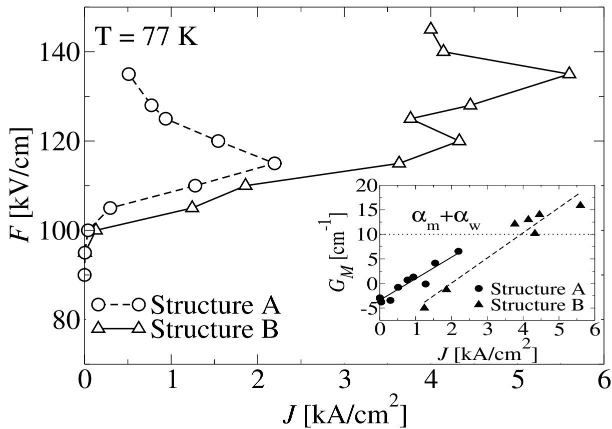

FIG. 1: Electric field versus current density characteristics. Inset: Modal gain as a function of current density. The horizontal dotted line shows the calculated total losses.

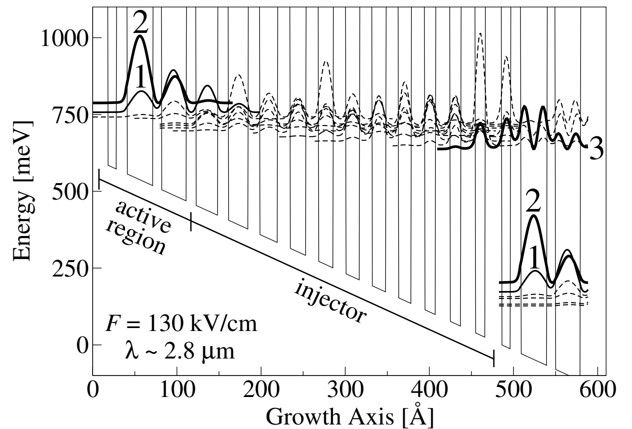

FIG. 2: Schematic conduction band diagram of structure B showing two active regions separated by an injector region. The moduli squared of the relevant wavefunctions are shown. The upper (3) and lower (2) laser levels are in bold and the uppermost miniband state (1) is shown as a solid line. The layer sequence of one period of the structure (in Å) starting from the injection barrier is: **21**/11/**11**/32/**10**/29/**13**/27/**13**/24/**13**/22/**14**/<u>20</u>/**14**/<u>18</u>/**14**/ <u>17</u>/**15**/<u>16</u>/**15**/<u>15</u>/**16** /<u>14</u>/**16**/13/**17**/13. The bold script denotes the $Al_{0.56}As_{0.44}Sb$ barriers, the normal script the $In_{0.53}Ga_{0.47}As$ wells. The underlined wells are doped with a sheet doping density of $N_s = 2.4 \times 10^{11}$ cm^{-2}. The calculated energy differences are $E_{32} = 435$ meV ($\sim$2.85 μm) and $E_{21} = 32$ meV (The LO-phonon energy of $In_{0.53}Ga_{0.47}As$ is 32.7 meV).

through the device and creating sufficient population inversion to achieve room-temperature lasing. To keep the emission wavelength in the same range as before, the triple quantum well active region (3QW) of structure A was used. In order to facilitate the efficient extraction of electrons from the active region and avoid a 'bottleneck' effect, the ground state was engineered to be part of the injector region miniband and hence utilise fast miniband transport for depopulation. Efficient injection into the upper laser level from the injector was ensured by engineering the upper laser level wavefunction to penetrate into the injector region, effectively becoming the lowest state in the injector miniband.

The design of structure B slightly differs from the 3QW vertical-transition scheme of structure A and becomes more of a 'miniband-to-bound' design. The laser transition takes place between the lowest state in the miniband and a bound state approximately one LO-phonon energy above the next miniband, ensuring that electrons are efficiently injected into the upper laser level and rapidly extracted from the lower laser level into the next period. The lower laser level is confined entirely in the right and central 3QW active region wells as opposed to the lower laser level in structure A which penetrates strongly into the first injector region well. This serves to increase the radiative transition element z_{32} (which is proportional to the local gain g) from 0.8 nm in structure A to 0.9 nm in structure B, even though the upper laser level in structure B penetrates further into the injector region miniband. The calculated subband populations for structure B at 77 and 300 K are shown in Table I. At a temperature of 77 K with a field of 130 kV/cm, structure B has a population inversion of 20% compared to the $\sim$2.6% inversion of structure A at the design field of 128 kV/cm. At 300 K the population inversion decreases to 8.4% at 130 kV/cm. The calculated F–J curve of structure B at 77 K is shown as the solid line in Fig. 1. The maximum total current density increases from 2.2 kA/cm^2 to 5.6 kA/cm^2 without significantly changing the applied bias or period length and keeping the same sheet doping density. This is due to the lack of an electron 'bottleneck' in the design and improved injection into the upper laser level. The sharp increase in current density at 120 kV/cm is due to the strong coupling between the bottom two miniband states at this value of field. The same waveguide implemented in structure A was used in the simulation of structure B. The modal gain increases by over 100% compared to structure A (see inset Fig. 1) leading to predicted laser emission at $\sim$2.8 μm. The threshold current is estimated at $\sim$4 kA/cm^2 with a calculated maximum operating temperature of 140 K.

In order to increase the modal gain G_M and achieve laser emission at higher temperatures, either the local gain g or mode confinement factor Γ must be increased. In order to increase Γ, a new plasmon-enhanced waveguide was designed, based upon the approach used by Yang *et al.* in their $\lambda \sim$4.5 μm InGaAs/AlAsSb QCL operating up to 400 K [5]. In this design, 30 periods of the active and injector regions of structure B are sandwiched between two 200 nm of $In_{0.53}Ga_{0.47}As$ confinement layers doped to 1×10^{17} cm^{-3}. The above layer sequence is surrounded on one side by an InP substrate and by three separate InP layers acting as waveguide cladding and contact layers on the other. Starting from the upper $In_{0.53}Ga_{0.47}As$ confinement layer, the InP layers doping densities and thicknesses are as follows: 5×10^{17} cm^{-3}, 20 nm; 2×10^{17} cm^{-3}, 1.3 μm; 7×10^{18} cm^{-3}, 1.3 μm. The mode confinement factor of the waveguide is calculated to be $\Gamma = 73\%$ with $\alpha_W = 0.73$ cm^{-1}. With this improved waveguide design, the maximum operating temperature of structure B was calculated to increase to 240 K.

To further increase G_M and hence the maximum operating temperature, a higher sheet doping density was used in the injector region to increase the local gain g. By increasing the sheet doping level from 2.4×10^{11} cm^{-2} to 3.8×10^{11} cm^{-2}, room temperature (300 K) laser emission was simulated. The relative subband populations at this higher doping are shown in Table I at 77 K and 300 K and are similar ($< 2\%$) to the relative populations at lower doping level. However, as the gain is approximately proportional to the dop-

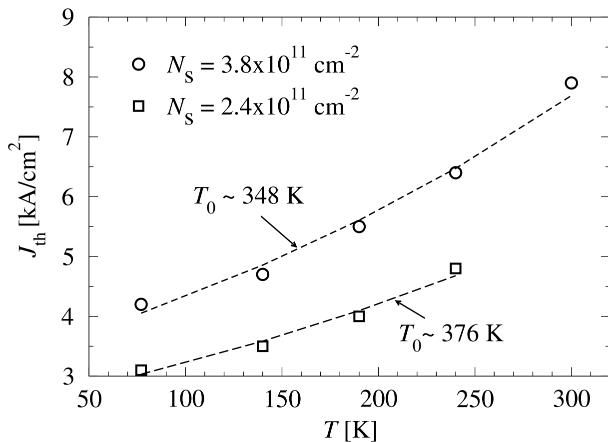

FIG. 3: Calculated threshold current densities as a function of temperature. The dashed lines show the exponential fits used to calculate the characteristic temperatures (T_0).

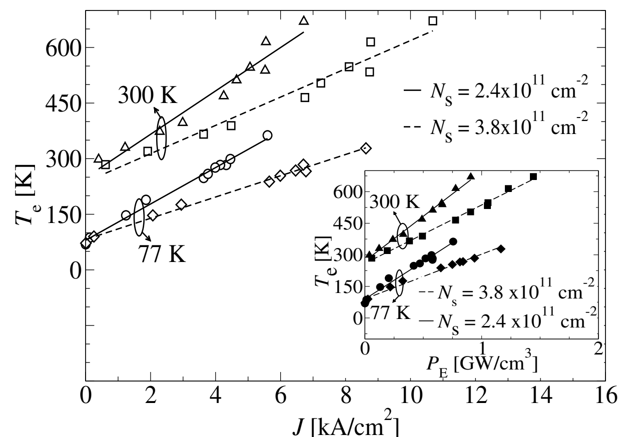

FIG. 4: Electron temperature as a function of current density at both doping densities and at lattice temperatures of 77 and 300 K. The coupling constants $\alpha_{e\text{–}l}$ were calculated from straight line fits to the data. Inset: Electron temperature as a function of electrical power density ($F \times J$). The straight line fits were used to calculate the coupling constants $\beta_{e\text{–}l}$.

ing level, overall the gain was found to increase by $\sim 50\%$. Fig. 3 shows the calculated temperature dependence of the threshold current of structure B at the different doping densities and the dashed lines represent the exponential fits used to calculate the characteristic temperatures (T_0) using the relation $J_{\mathrm{th}} \approx J_{\mathrm{th}}(0)\exp(T/T_0)$.

The electron temperature as a function of current density for structure B was calculated at both injector sheet doping densities and is shown in Fig. 4 at lattice temperatures of 77 and 300 K. At 77 K a linear dependence was obtained although at the higher lattice temperature there is evidence of an exponential increase in electron temperature with current density, but this can be reasonably approximated as quasi-linear. The electron–lattice coupling constants ($\alpha_{e\text{–}l}$) were deduced from straight line fits to the data [8]. At the lower sheet doping density ($N_s = 2.4\times10^{11}$ cm^{-2}) $\alpha_{e\text{–}l}$ was calculated to be equal to 49.1 and 58.5 K/kA cm^{-2} at 77 and 300 K respectively. These values are slightly lower than the calculated coupling constants of structure A (53.7, 61.5 K/kA cm^{-2} at 77, 300 K) indicating no degradation in electron heating. When the sheet doping density was increased to 3.8×10^{11} cm^{-2}, the coupling constants decreased to 28.9 K/kA cm^{-2} at 77 K and 38.16 K/kA cm^{-2} at 300 K.

A quasi-linear relationship was also found between the electron temperature and the electrical power density ($P_E = F \times J$), even at 300 K (see inset Fig. 4). The relationship is of the form $T_e = T_l + \beta_{e\text{–}l}P_E$ with the coupling constant $\beta_{e\text{–}l}$ obtained from straight line fits to the data. At 77 K, $\beta_{e\text{–}l}$ has values of 0.36 and 0.21 K/MW cm^{-3} at the lower and higher sheet doping densities respectively. At 300 K the corresponding values of $\beta_{e\text{–}l}$ are 0.43 K/MW cm^{-3} and 0.28 K/MW cm^{-3}. The values of both $\alpha_{e\text{–}l}$ and $\beta_{e\text{–}l}$ decrease as the sheet doping density increases due to the higher number of electrons in the device. At a higher doping density, a smaller applied bias generates the same current density as a larger applied bias at a lower doping density. Hence for a given current density, the power of each individual electron is lower at the higher doping density and therefore less electron heating occurs. This was confirmed by calculating the ratio between the relative increase in electron temperature and the power of each individual electron $(T_e - T_l)/(P_E/N_s)$ which is equivalent to $\beta_{e\text{–}l}N_s$ and shows almost constant behaviour for both doping levels.

In conclusion, the simulation and design of InGaAs/AlAlSb QCLs has been reported using a fully self-consistent rate equation model. For the designed QCL a large population inversion was predicted, which in conjunction with the suggested improvements in the waveguide design, yields sufficient gain for the possibility of laser action up to at least 300K. Considerable electron heating is anticipated, reflected by the large electron temperature–current density coupling constants of average value ~ 55 K/kA cm^{-2} which are twice as large as those found in mid-infrared GaAs-based QCLs.

---

[1] D. G. Revin, M. J. Steer, L. R. Wilson, R. J. Airey, J. W. Cockburn, E. A. Zibnik, and R. P. Green, Electron. Lett. **40**, 874 (2004).

[2] D. G. Revin, L. R. Wilson, E. A. Zibnik, R. P. Green, J. W. Cockburn, M. J. Steer, R. J. Airey, and M. Hopkinson, Appl. Phys. Lett. **84**, 1447 (2004).

[3] D. G. Revin, L. R. Wilson, E. A. Zibnik, R. P. Green, and J. W.Cockburn, Appl. Phys. Lett. **85**, 3992 (2004).

[4] Q. Yang, C. Manz, W. Bronner, K. Köhler, and J. Wagner, Electron. Lett. **40**, 1339 (2004).

[5] Q. Yang, C. Manz, W. Bronner, C. Mann, L. Kirste, K. Köhler, and J. Wagner, Appl. Phys. Lett. **86** (2005).

[6] D. Indjin, P. Harrison, R. W. Kelsall, and Z. Ikonić, Appl. Phys. Lett. **82**, 1347 (2003).

[7] P. Harrison, *Quantum Wells, Wires, and Dots: Theoretical and Computational Physics* (Wiley, Chichester, 1999).

[8] P. Harrison, D. Indjin, and R. W. Kelsall, J. Appl. Phys. **92**, 6921 (2002).

[9] N. Georgiev and T. Mozume, J. Appl. Phys. **89**, 1064 (2001).

[10] N. Susa, IEEE J. Quantum Electron. **32**, 20 (1996).

[11] J. Stiens, R. Vounckx, I. Veretennicoff, A. Voronko, and G. Shkerdin, J. Appl. Phys. **81**, 1 (1997).